

Pointing with the wrist: a postural model for Donders' law

Domenico Campolo · Ferdinan Widjaja ·
Mohammad Esmaeili · Etienne Burdet

the date of receipt and acceptance should be inserted later

Abstract The central nervous system uses stereotypical combinations of the three wrist/forearm joint angles to point in a given (2D) direction in space. In this paper, we first confirm and analyze this Donders' law for the wrist as well as the distributions of the joint angles. We find that the quadratic surfaces fitting the experimental wrist configurations during pointing tasks are characterized by a subject-specific Koenderink shape index, and by a bias due to the prono-supination angle distribution.

We then introduce a simple postural model using only four parameters to explain these characteristics in a pointing task. The model specifies the redundancy of the pointing task by determining the one-dimensional task-equivalent manifold (TEM), parameterized via wrist torsion. For every pointing direction, the torsion is obtained by the concurrent minimization of an extrinsic cost, which guarantees minimal angle rotations (similar to Listing's law for eye movements), and of an intrinsic cost, which penalizes wrist configurations away from comfortable postures. This allows simulating the sequence of wrist orientations to point at eight peripheral targets, from a central one, passing through intermediate points.

The simulation results first show that in contrast to eye movements, which can be predicted by only considering the extrinsic cost (i.e. Listing's law), both costs are necessary to account for the wrist/forearm experimental data. Second, fitting the synthetic Donders' law from the simulated task with a quadratic surface yields similar fitting errors compared to experimental data.

D. Campolo, F. Widjaja, M. Esmaeili
School of Mechanical and Aerospace Engineering,
Nanyang Technological University, 639798 Singapore.
Tel.: +65 6790 5610
Fax: +65 6792 4062
E-mail: d.campolo@ntu.edu.sg

E. Burdet
Department of Bioengineering, Imperial College London, SW7 2AZ London, UK.

Third, if concurrent minimization of intrinsic and task-related costs holds, then the assessment of the relative involvement of the wrist joints in a redundant task would indicate how those costs are weighted.

Keywords Human Wrist · Kinematic Redundancy · Donders’ law · Hopf Fibration · Multi-Objective Optimization

1 Introduction

Pointing with the human wrist, like gazing with the eye, is a kinematically redundant task, as infinite postures can be used to point in a given direction. How does the central nervous system (CNS) deal with this indeterminacy? Since the nineteenth century, studies on eye movements have shown the existence of simplifying strategies adopted by the brain when dealing with kinematically redundant problems.

In particular, Donders [8] showed that for any steady gazing direction, the human eye assumes the same combination of elevation, azimuth and torsion angles. *Donders’ law* states that in the three dimensional space of possible eye configurations, the physiological eye configurations are constrained to a two-dimensional surface now called *Donders’ surface*.

When representing eye orientation by a rotation vector relative to the subject-dependent *primary position* (approximately corresponding to gazing straight ahead), Donders’ surface appears as a plane normal to the primary position: The eye assumes only those postures that can be reached from the primary position by a single rotation about an axis in this *Listings plane* [24]. In the last two decades, advanced technologies have allowed verifying this *Listing’s law* during fixation as well as during saccade movements, smooth pursuit, and vergence [25].

The existence of a constrained behavior such as Donders’ law in a mechanically unconstrained system indicates a sensorimotor strategy. For eye movements, where torsion is not under voluntary control, it was long debated whether Listing’s law is due to a biomechanical or to a neural mechanism. It is now known that no such law holds during sleep, suggesting that Listing’s law is actively implemented by a neural mechanism [25].

Like the eye, the wrist has 3 degrees-of freedom (dof), i.e. pronosupination, flexion-extension and radial-ulnar deviation, which have approximately perpendicular but non-intersecting axes [18]. While the human wrist has obvious anatomical differences to the oculomotor system, a similar control mechanism may be used by the CNS for these two systems with similar kinematics [15].

We recently investigated wrist movements using a dedicated apparatus [3]. Experimental data of 3D wrist orientations during a pointing task with the wrist (and expressed in the *standard coordinates* based on rotation vectors as described above) were fitted with a quadratic surface. The fit was evaluated in terms of the *surface thickness* defined as the standard deviation of its residuals. The data showed good fit with thickness between 1-2 degrees, exhibiting

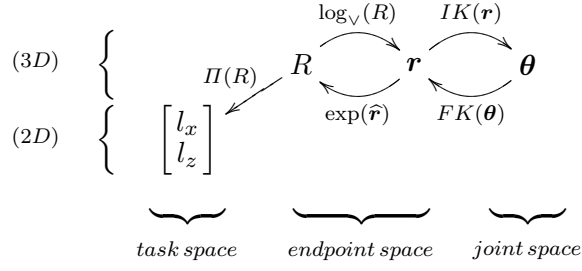


Fig. 1 Commutative diagram of the mappings between spaces. The three-dimensional joint and endpoint spaces fully describe the wrist configuration, and project via $\Pi(R)$ to the (two-dimensional) task space with screen coordinates $[l_x \ l_z]^T$. The orientations in the endpoint space can be represented either in terms of rotation matrices (R , which can be more practically related to the pointing task) or rotation vectors (\mathbf{r} , which provides an intuitive and more compact representation).

Donders' surfaces for the wrist with subject-specific curvature, possibly due to individual biomechanical factors.

While, in standard coordinates, Donders' surface appears to be planar for the eyes, it is twisted for the arm [16] and the head [4], corresponding to a Fick gimbal strategy. In the experiments described by Ceylan et al. [4], when head and gaze were associated, different forms of Donders law held, switching from Fick-like to planar surfaces according to the tasks. On the other hand, when head motion was disassociated from gaze, the motor strategy was shown to be path-dependent, i.e. incompatible with any Donders' law.

Does the CNS control the wrist in a manner similar to the eye, to the arm, or in a different way? This paper investigates the wrist control by developing a simple phenomenological model to explain Donders' law for wrist postures. This model considers both extrinsic (task-related) factors, as have been used to model the eye kinematics, and intrinsic (joint-related) factors, as have been used for the arm. The extrinsic costs are associated with task-related factors, such as the amount of rotation required to redirect gaze. The cost associated with extrinsic factors is assumed to be the same for all subjects, while the cost associated with intrinsic factors, depending on the wrist kinematics and the range of each dof, is parameterized to account for subject-specific biomechanical factors.

In the following sections, we first derive a kinematic model for the wrist and deploy geometric tools to analyze the redundancy in pointing tasks. We then analyze experimental data on pointing tasks with the wrist, which will be used to test the model. We compare, in terms of curvature of Donders' surfaces, the experimental data with the family of synthetic Donders' laws generated by the model, and discuss the predictive features of our proposed model. Finally, we also discuss a possible relationship between Listing's law for the eyes and Donders' law for the wrist.

2 Model

2.1 Wrist Kinematics

Wrist motions are analyzed in three different spaces: joint, endpoint and task spaces, which will be defined below (Fig. 1). The transformations between these spaces are detailed in the Appendix.

2.1.1 Joint space (3D)

The human wrist can be modeled as a 3dof system comprising the following rotational joints¹ (from proximal to distal): pronosupination (PS), flexion-extension (FE), and radial-ulnar deviation (RUD). While FE and RUD are anatomically confined within the wrist, the latter being the most distal [1], the forearm PS is due to the articulated complex between elbow and wrist. We assume that these joints are characterized by the angles θ^{RUD} , θ^{FE} and θ^{PS} confined to a biomechanical range. We group these angles in a 3D vector $\boldsymbol{\theta} := [\theta^{RUD} \ \theta^{FE} \ \theta^{PS}]^T$, which are the coordinates of the *joint space*.

2.1.2 Endpoint space (3D)

The *endpoint space* is constituted by the spatial orientations of the wrist with respect to the anatomical *neutral configuration* [26]. Given an orthonormal fixed frame $\{\mathbf{e}_x; \mathbf{e}_y; \mathbf{e}_z\}$ (pointing respectively forward, left and up), a moving orthonormal frame $\{\mathbf{e}_1; \mathbf{e}_2; \mathbf{e}_3\}$, attached to the hand, is uniquely defined as to coincide with the fixed frame in the neutral configuration. At any time, the components of the moving frame in fixed frame coordinates are given by

$$\mathbf{e}_1 = R \begin{bmatrix} 1 \\ 0 \\ 0 \end{bmatrix}, \quad \mathbf{e}_2 = R \begin{bmatrix} 0 \\ 1 \\ 0 \end{bmatrix}, \quad \mathbf{e}_3 = R \begin{bmatrix} 0 \\ 0 \\ 1 \end{bmatrix} \quad (1)$$

where R is a 3×3 rotation matrix R (the identity matrix corresponds to the neutral configuration).

While the matrix representation is practical to combine different orientations, a geometrically more intuitive representation of orientation is provided using a *rotation vector*: a rotation can be represented by the vector \mathbf{r} pointing in the direction of the rotation axis with magnitude $|\mathbf{r}|$ corresponding to the rotation angle. Vector and matrix representations are related, as described in the Appendix, by the Lie groups exponential (A-1) and logarithmic (A-2) maps.

¹ Anatomically speaking, only flexion-extension and radial-ulnar deviation are part of the wrist, while pronation-supination is part of the forearm, but functionally they all contribute to the final 3D orientation of the hand.

2.1.3 Forward and inverse kinematics

The joint and endpoint spaces are related through forward and inverse kinematic transformations. To any given set of values for the joint angles (within the joint limits) there corresponds a unique wrist configuration, yielding the *forward kinematic transformation* $\mathbf{r} = FK(\boldsymbol{\theta})$, defined in (A-4). Similarly, any physiological configuration of the wrist is realized by a unique combination of joint angles, yielding the *inverse kinematic transformation* $\boldsymbol{\theta} = IK(\mathbf{r})$ defined in (A-5)².

2.1.4 Task space (2D)

A hand-held laser aligned with \mathbf{e}_1 , pointed in a direction $\mathbf{n} = R\mathbf{e}_x$ ($|\mathbf{n}| = 1$) towards a vertical screen in the yz -plane, would hit the screen at coordinates:

$$\begin{bmatrix} l_y \\ l_z \end{bmatrix} = \Pi(R) := \begin{bmatrix} 0 & -1 & 0 \\ 0 & 0 & 1 \end{bmatrix} R \begin{bmatrix} 1 \\ 0 \\ 0 \end{bmatrix}, \quad (2)$$

assuming the origin of the screen at unit distance from the wrist along \mathbf{e}_x and the y -axis of the screen directed as $-\mathbf{e}_y$.

2.2 Task-equivalent manifold (TEM)

We wish to determine all possible wrist configurations R aligning the moving frame \mathbf{e}_1 to a direction \mathbf{n} ($|\mathbf{n}| = 1$). From (1) we have

$$\mathbf{n} \equiv \mathbf{e}_1 = R[1 \ 0 \ 0]^T. \quad (3)$$

One solution to (3) is represented by the ‘Listing’s rotation’, defined as the rotation which brings \mathbf{e}_x onto \mathbf{n} through a *minimum* angle $0 \leq \theta < \pi$, i.e. a rotation acting along the axis parallel to $\mathbf{e}_x \times \mathbf{n}$. Since $|\mathbf{e}_x \times \mathbf{n}| = \sin \theta$ and $\mathbf{e}_x \cdot \mathbf{n} = \cos \theta$, the rotation vector³ \mathbf{r}_L that generates the Listing rotation is

$$\mathbf{r}_L(\mathbf{n}) := \frac{\mathbf{e}_x \times \mathbf{n}}{\sin \theta} \theta = \frac{\mathbf{e}_x \times \mathbf{n}}{|\mathbf{e}_x \times \mathbf{n}|} \arctan \left(\frac{|\mathbf{e}_x \times \mathbf{n}|}{\mathbf{e}_x \cdot \mathbf{n}} \right) \quad (4)$$

For further calculations, we then define a *Listing operator*

$$\mathcal{L}_{\mathbf{e}_x}(\mathbf{n}) := \exp(\widehat{\mathbf{r}_L}(\mathbf{n})) \quad (5)$$

² In general, wrist joint of mechanical systems involve singularities, however the restriction to physiological range of motion of the human wrist joints (Table 1) allows using singularity-free transformations.

³ Definition (4) is ambiguous whenever $\mathbf{n} = \pm \mathbf{e}_x$. However $\mathbf{n} = -\mathbf{e}_x$ is out of the physiological range, as it corresponds to a π radians rotation. The case $\mathbf{n} = \mathbf{e}_x$ corresponds to $\theta = 0$ and since $|\mathbf{r}_L| = \theta$, we assume by continuity that $\mathbf{r}_L = 0$ whenever $\theta = 0$.

via the exponential map of eq. (A-1), where $\mathbf{r}_L(\mathbf{n})$ is defined in (4) and the *hat* symbol $\hat{\cdot}$ is defined in the Appendix. For a given \mathbf{n} , the Listing operator returns the rotation matrix which brings \mathbf{e}_x onto \mathbf{n} through a ‘minimal’ rotation.

The *task equivalent manifold* (TEM) of all rotations pointing to a direction can be formed by adding to the Listing’s rotation a *cyclorotation* $R_C = \exp(\hat{\mathbf{e}}_x \tau)$ about the pointing direction, where τ is the *torsion* amount [12]. Any general wrist configuration R pointing towards a direction \mathbf{n} as in (3) differs from the Listing’s rotation $\mathcal{L}_{\mathbf{e}_x}(\mathbf{n})$ by a cyclorotation, i.e.

$$\mathcal{L}_{\mathbf{e}_x}(\mathbf{n}) \exp(\hat{\mathbf{e}}_x \tau) = R. \quad (6)$$

In this notation, $\tau = 0$ corresponds to a Listing’s rotation, which is also referred to as zero-torsion.

Equation (6) allows decomposing a general rotation matrix into a cyclorotation followed by a Listing’s rotation. In terms of rotation vectors $\log_v(R)$ as defined in (A-2), the TEM to the pointing direction \mathbf{n} is

$$\text{TEM}_{\mathbf{e}_x}(\mathbf{n}) := \{\log_v(\mathcal{L}_{\mathbf{e}_x}(\mathbf{n}) \exp(\hat{\mathbf{e}}_x \tau)) : -\pi \leq \tau \leq \pi\}. \quad (7)$$

Remark: The configuration space of the human wrist is a subset of the solid ball of radius π in the space of rotation vectors. The space of all possible pointing directions \mathbf{n} can be identified with the two-sphere since $|\mathbf{n}| = 1$. For each pointing direction \mathbf{n} , we identify $\text{TEM}_{\mathbf{e}_x}(\mathbf{n})$ from (7), which yields a one dimensional manifold or *fiber* parameterized via the torsion [12]. As $\tau = \pm\pi$ generate the same rotation, each fiber is actually a closed loop. The space of 3D rotations can therefore be seen as the product between a two-sphere and a circle, the so-called Hopf fibration [19].

2.3 Multi-objective optimization

Our model considers two kinds of costs, namely extrinsic cost (corresponding to Listing’s law) and intrinsic cost (corresponding to avoiding uncomfortable postures), as explained below.

2.3.1 Extrinsic cost

Since the early explanations by von Helmholtz in terms of ‘easiest orientation’, various other accounts have been given to explain Listing’s law in terms of optimization of purely visual or sensorimotor performance (see [13] and references therein). It can be shown that Listing’s law corresponds to minimizing

$$\mathcal{C}_{extr}(\mathbf{r}) := |\mathbf{r}|^2 \quad (8)$$

while constraining \mathbf{r} to represent the rotation which brings \mathbf{e}_x onto a given pointing direction.

As highlighted in [9], knowing the TEM for a given pointing direction \mathbf{n} is computationally beneficial since an *unconstrained* minimization of the cost function

$$\mathcal{C}_{extr}(\tau) = |\log_{\vee}(\mathcal{L}_{\mathbf{e}_x}(\mathbf{n}) \exp(\widehat{\mathbf{e}}_x \tau))|^2$$

can be carried out over the (scalar) torsion τ instead of solving a constrained extremal problem in 3D. A simple algebraic computation shows that the minimum occurs for $\tau = 0$, i.e. for Listing's rotation vector \mathbf{r}_L . By construction, see (4), \mathbf{r}_L is always perpendicular to \mathbf{e}_x . Therefore, for all \mathbf{n} , the Listing's rotation vectors \mathbf{r}_L lie on the vertical plane perpendicular to \mathbf{e}_x , i.e. Listing's law.

2.3.2 Intrinsic cost

Based on the intrinsic costs proposed by Pennestrì et al. [21], we define a family of non-negative, U-shaped discomfort functions whose minimum (most comfortable position) occurs at $\theta_{off} + \theta_0$, typically around the middle of the range of motion:

$$f(\theta) := \left(\frac{\theta - \theta_{off} - \theta_0}{\Delta\theta_0} \right)^4 \quad \text{where} \quad \begin{cases} \theta_0 = \frac{\theta_{max} + \theta_{min}}{2} \\ \Delta\theta_0 = \frac{\theta_{max} - \theta_{min}}{2} \end{cases} \quad (9)$$

We define this cost joint by joint and consider an overall discomfort function by summing up the discomfort values at each joint:

$$F_{intr}(\boldsymbol{\theta}) := f(\theta^{RUD}) + f(\theta^{FE}) + f(\theta^{PS}) \quad (10)$$

2.3.3 Optimization

To consider the intrinsic and extrinsic costs simultaneously, we remap intrinsic costs from joint to endpoint space using:

$$\mathcal{C}_{intr}(\mathbf{r}) := F_{intr}(IK(\mathbf{r})). \quad (11)$$

The overall cost is defined as the combination of extrinsic and intrinsic costs

$$\mathcal{C}_{tot}(\mathbf{r}) := (1 - \lambda) \mathcal{C}_{intr}(\mathbf{r}) + \lambda \mathcal{C}_{extr}(\mathbf{r}), \quad (12)$$

where $0 \leq \lambda \leq 1$ is a parameter weighting the two costs.

For any pointing direction \mathbf{n} , the optimal rotation is obtained from the torsion minimizing (12):

$$\begin{cases} \tau^{opt} := \underset{-\pi \leq \tau \leq \pi}{\operatorname{argmin}} \mathcal{C}_{tot}(\log_{\vee}(\mathcal{L}_{\mathbf{e}_x}(\mathbf{n}) \exp(\widehat{\mathbf{e}}_x \tau))) , \\ \mathbf{r}^{opt} := \log_{\vee}(\mathcal{L}_{\mathbf{e}_x}(\mathbf{n}) \exp(\widehat{\mathbf{e}}_x \tau_{opt})) . \end{cases} \quad (13)$$

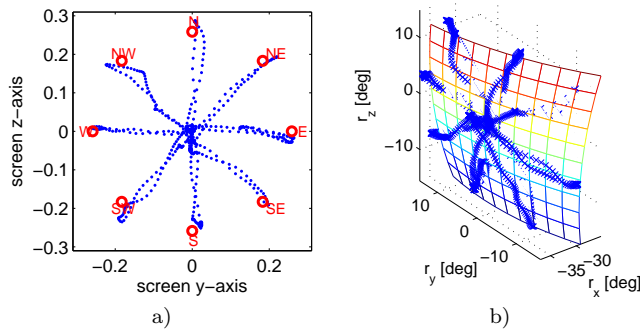


Fig. 2 One trial performed by a representative subject with screen coordinates trajectories (a) and as in the rotation vectors space (b).

3 Experiments

3.1 Point-to-point experiment

Experiments similar to [3] were conducted to provide data for testing the model. Eight healthy subjects with no known history of neuromuscular impairment, who declared to be right-handed and gave their informed consent, performed a pointing task from a central target towards one of eight targets 15° away from the center and oriented at $\{0^\circ, 45^\circ, 90^\circ, 135^\circ, 180^\circ, 225^\circ, 270^\circ, 315^\circ\}$ ([3], Fig. 2a). Each *trial* consisted of eight back and forth movements to the targets in random sequence. Each subject performed ten consecutive trials.

Throughout the experiment, each subject was strapped to a chair to restrain all torso and upper-limb motions except the ones of interest (FE, RUD and PS for the wrist). To acquire data, each subject would grasp a lightweight handle, sensorized with an orientation tracking sensor (MTx-28A-33-G25 device from XSens Inc. with $< 1^\circ$ static orientation accuracy and 40Hz bandwidth. Before starting each trial, a zeroing-procedure was carried out, defining the anatomically neutral position for the wrist as the initial one (by default, such a zero-position would point towards the central target), see [3] for details. Data at 120Hz were downloaded onto a local PC for offline data analysis. Real-time visual feedback of the current pointing position was provided during movement.

3.2 Data Analysis

Data acquired from each trial consisted of a sequence R_i of 3×3 rotation matrices (i being sample number with 100 samples per second). For each trial, we computed the sequence of corresponding rotation vectors $\mathbf{r}_i = [r_{xi} \ r_{yi} \ r_{zi}]^T := \log_{\vee}(R_i)$. Then we fitted the sequence of the first components r_{xi} to a quadratic

function [3]:

$$r_{xi}^* = C_1 + C_2 r_{yi} + C_3 r_{zi} + C_4 r_{yi}^2 + 2C_5 r_{yi} r_{zi} + C_6 r_{zi}^2 \quad (14)$$

which defines the *Donders' surface*, as well as the *thickness* defined as the standard deviation of the residuals $x_{xi}^* - x_{xi}$. C_1 , C_2 , and C_3 are indicative of linear features such as tilt and offset of the surface in 3D space, while C_4 , C_5 , and C_6 are related to the surface's curvature. A more standard goodness of fit index is provided by the *variance accounted for*

$$\text{VAF} := \left(1 - \frac{\text{var}(r_i^* - r_i)}{\text{var}(r_i)}\right) 100\%, \quad (15)$$

which was also computed relatively to the fitting of each trial for all subjects. Fig. 2b shows an example of fitting of experimental data for a representative subject.

The *mean curvature*, i.e. the mean of largest and smallest section curvatures, expressed in the C_i coefficients as [7], [3]

$$H = \frac{(2 + 2C_3^2)C_4 - 4C_3C_2C_5 + (2 + 2C_2^2)C_6}{2(1 + C_2^2 + C_3^2)^{3/2}}, \quad (16)$$

and the *Gauss curvature*, corresponding to their product and expressed in the C_i coefficients as [7], [3]

$$K = \frac{4C_4C_6 - 4C_5^2}{(1 + C_2^2 + C_3^2)^2}, \quad (17)$$

are used to analyze the *geometric invariant features* of Donders' surfaces near the origin. We employ Koenderink's Shape Index [17]

$$S = -\frac{2}{\pi} \arctan \frac{H}{\sqrt{H^2 - K}} \quad (18)$$

to analyze the 'shape' of Donders' surfaces. Koenderink's index captures the intuitive notion of shape independent of the curvature amount, e.g. two spheres of different radii have same shape index but different amounts of curvature. By definition $-1 \leq S \leq 1$.

3.3 Simulated experiment

The experiment of Section 3.1 is simulated, where the 'path' is computed at angles $\phi = 1^\circ, 2^\circ, \dots, 15^\circ$, yielding $8 \times 15 + 1 = 121$ targets (also considering the central one) (Fig. 3a). For each target \mathbf{n}_i ($i = 1, 2, \dots, 121$) there corresponds a set of rotation vectors identified by $\text{TEM}_{e_x}(\mathbf{n}_i)$ and, among which the optimal torsion τ_i^{opt} and rotation vector $\mathbf{r}_i^{\text{opt}}$ are computed by solving eq. (13) (using the MATLAB function `fminunc` to compute *argmin*). The range of motion for the wrist joint angles might differ from subject to subject, but is assumed to be as in Table 1.

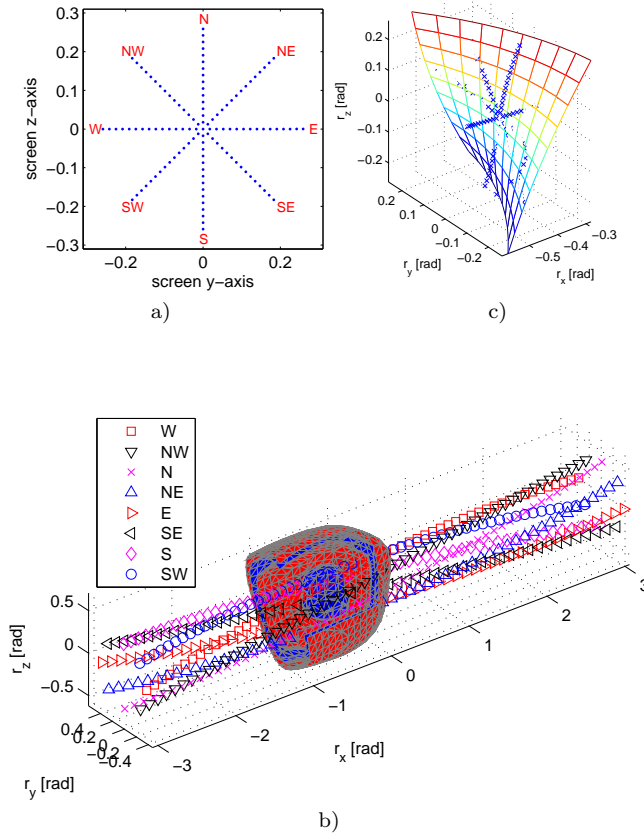


Fig. 3 Simulated point to point movements. a) Peripheral and intermediate set of pointing targets in screen coordinates. b) Task equivalent manifold fibers relative to the peripheral targets (denoted by different markers) intersecting a family of isosurfaces (only 4 isosurfaces are visible through a section) for a total cost relative to $\lambda = 0.02$, with $\theta_{off}^{PS} = 40^\circ$ and $\theta_{off}^{FE} = \theta_{off}^{RUD} = 10^\circ$ for the discomfort functions at each joint. c) Optimal rotation vectors (crosses) and quadratic surface fit to these parameters.

angle	min	max	unit
θ_{off}^{RUD}	-50	35	deg
θ_{off}^{FE}	-65	70	deg
θ_{off}^{PS}	-90	90	deg

Table 1 Range of motion for the wrist joint angles.

Fig. 3b shows, in the endpoint space, the $TEM_{e_x}(\mathbf{n}_i)$ fibers relative to the peripheral targets as well as the cost ‘isosurfaces’, i.e. surfaces for which every point has a constant cost ($\mathcal{C}_{tot} = const$). The cost isosurfaces have a smooth

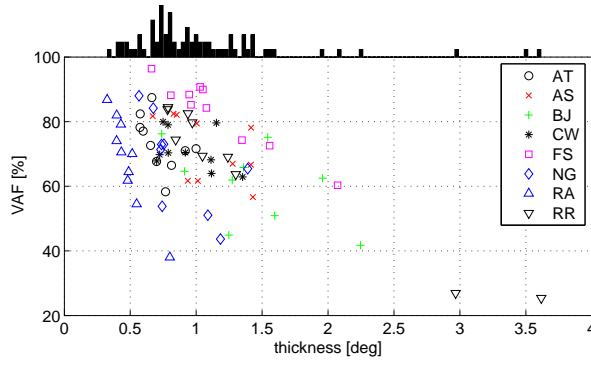


Fig. 4 Variance accounted for (VAF) vs. thickness for each trial for all subjects. Specific markers are used for the different subjects.

and concentric shell-like structure⁴, with the cost increasing from internal to the external shells. For each fiber $\text{TEM}_{e_x}(\mathbf{n}_i)$, the optimal rotation vector $\mathbf{r}_i^{\text{opt}}$ in (13) corresponds to the tangent of $\text{TEM}_{e_x}(\mathbf{n}_i)$ with the isosurface.

Similarly to what was done with the experimental data, once all the optimal wrist configurations $\mathbf{r}_i^{\text{opt}}$ ($i = 1, 2, \dots, 121$) were available for all targets, Donders' law was quantified in terms of best fitting quadratic surface. Fig. 3c shows the optimal rotation vectors and the fitted quadratic function for the specific case of Fig. 3b, where the following parameters were used: $\lambda = 0.02$ for the total cost (12), 40° offset for the PS joint, 10° offset for both FE and RUD joints.

4 Results

4.1 Experimental Results

4.1.1 Thickness distribution

Data from each single trial were fitted with the generic quadratic surface of eq. (14). As in [3], for most of the trials and in most of the subjects, the thickness was around 1° : 0.9° median and 1.0° mean value. Fig. 4 displays the relationship between the thickness and the variance accounted for (VAF) index relatively to the fitting of each trial for all subjects.

Fig. 5 shows the Donders' surfaces relative to all trials, for each subject. From a visual inspection, two major features appear. The first is that inter-subject differences can be appreciated in terms of curvature of Donders' surfaces, confirming [3]. The second feature, not addressed in previous studies,

⁴ The isosurfaces of extrinsic costs eq. (8) are concentric spheres in the end-point space. The isosurfaces of discomfort functions are ellipsoids in the joint-space ($F_{\text{intr}}(\boldsymbol{\theta}) = \text{const}$). When mapped back to the end-point space via the inverse kinematics map, the smooth and concentric shell-like structure is maintained since $IK(\mathbf{r})$ is a smooth mapping and eq. (12) is linear.

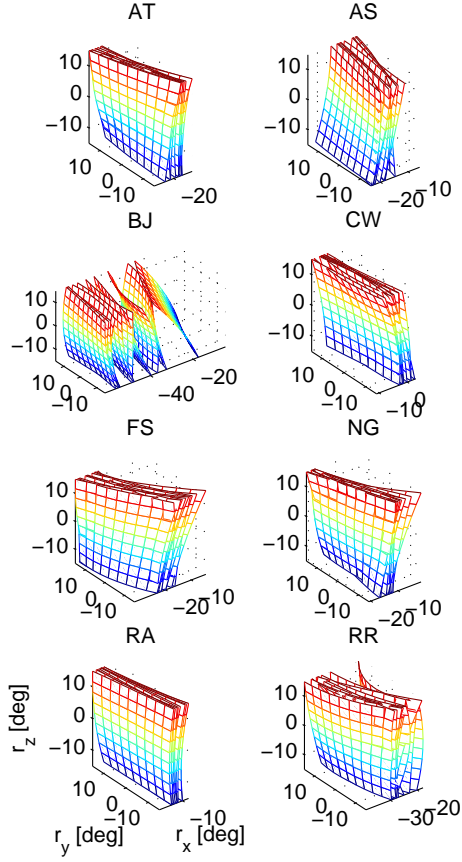


Fig. 5 Donders' surfaces of all trials for each subject.

is that besides shape, the surfaces seem to be characterized by an 'offset' in the r_x component, corresponding to an offset in prono-supination (note: when pointing at the central target, $r_y = r_z = 0$, then $r_x = -\theta^{PS}$).

4.1.2 Curvature and shape analysis

Fig. 6a shows Gauss curvature K as a function of mean curvature H , for all trials of all subjects. Note that, as H is the mean of the minimal and maximal one-dimensional curvature and K is its product, (H, K) pairs can only assume values in the region $K \leq H^2$. This plot reveals between-subjects differences in terms of curvature. The dotted lines in Fig. 6a show the *loci* of the equivalent Shape Index, suggesting subject-specific clustering in terms of shape. Indeed, Fig. 6b illustrates subject specific distributions of shape index. In most of the trials and subjects, the Donders' surfaces have a negative shape index ($p < 10^{-6}$, t-test).

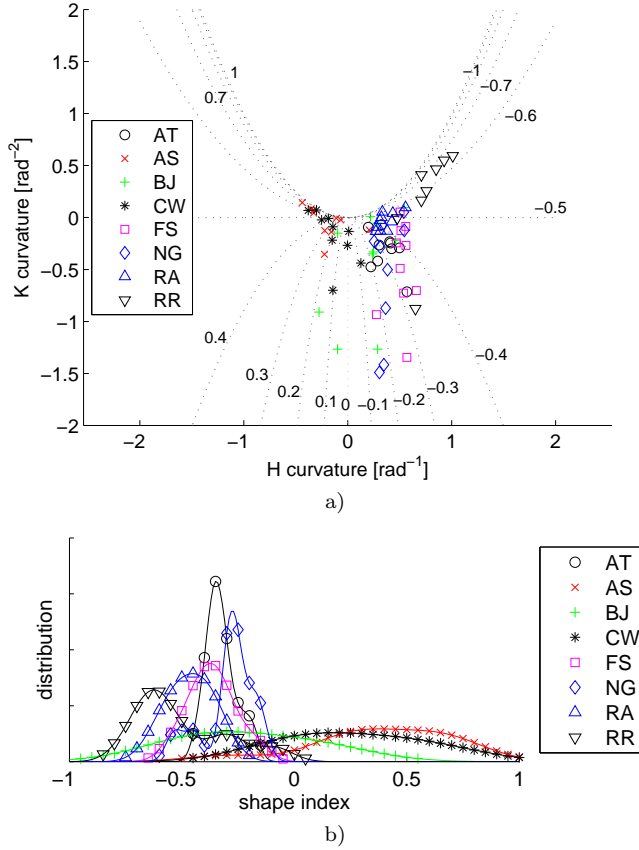


Fig. 6 a) Mean curvature (H) vs. Gaussian curvature (K) for all trials and all subjects. The different subjects are indicated with specific markers, as indicated in the legend. Dotted lines indicate *loci* of (H, K) pairs with same Shape Index. b) Distribution of shape index eq. (18) for all subjects.

To further investigate inter-subjective differences in terms of shape, we performed a non-parametric analysis of variance (Kruskal-Wallis test) for all trials, using the shape index as dependent variable and the subjects as grouping factor. This highlighted statistical differences ($p < 10^{-7}$) for the median of the groups. Based on Kruskal-Wallis statistics (using the Matlab7.1 `multcompare` function), pairwise comparisons were also performed, which showed between-groups differences (at 95% confidence level). Except for subjects 'NG' and 'BJ', all other subjects have Shape Index distributions which are significantly different (95% confidence level) from at least another subject.

4.1.3 Prono-supination offset

To analyze the PS joint offset, we used the inverse kinematics of the wrist model (A-5) to estimate joint angles from the experimental wrist orientations. Fig. 7a shows the distribution (estimated for each joint angle via the `ksdensity` function in Matlab 7.1) of the three joint angles (columns) for each subject (rows), superimposing all the trials for each subject (each solid line represents the distribution for a single trial). It is clear that RUD and FE have a similar and roughly symmetric distribution both within- and between-subjects (no statistical difference was detected for either mean or standard deviation of the distributions for RUD and FE by a Kruskal-Wallis test, using subjects as grouping factor).

The task redundancy becomes evident when analyzing the PS joint (third column of Fig. 7a). A large variability is observed in terms of both mean and standard deviation of the PS joint angle. In particular, a Kruskal-Wallis test detected statistical differences for the PS joint distribution both in terms of mean ($p \leq 10^{-13}$) and standard deviation ($p \leq 10^{-9}$) when using subjects as grouping factor. To better appreciate these differences, Fig. 7b shows the mean vs. standard deviation of the PS joint angle distribution for all subjects.

4.2 Results from the model

The above experimental results, in particular the angular deviation exhibited in Fig. 7, motivated modeling as described in Section 2. We investigated in simulations the influence of variation of parameters such as λ in (12) and the θ_{off} in (9) for each of the three joints (namely θ_{off}^{FE} , θ_{off}^{RUD} and θ_{off}^{PS}). The offset parameter of each joint angle was systematically varied within a subset of its physiological range of motion ($\pm 20^\circ$ for FE and RD and $\pm 40^\circ$ for PS), as well as the parameter λ between its definition limits ($0 \leq \lambda \leq 1$). For each combination of parameters, an optimal solution as described in Section 3.3 was derived and fit with a quadratic surface.

Thickness distribution: The synthetic Donders' law relative to each combination of parameters, once fitted with a quadratic surface, exhibits a non-negligible thickness similar to the real data. Fig. 8 shows the normalized distribution of the thickness values for the simulated variations of parameters. Most of the values for thickness are around 1° , with 0.8° median and 1.3° mean value.

Curvatures distribution: Systematic variation of the four model's parameters (λ and the three offsets of the joint angles) showed that the model can produce surfaces with H and K curvatures spanning the whole HK plot in Fig. 6-a and beyond, in particular accounting for the experimental data. Heuristically, we noticed that the experimental data correspond to a small range of parameters values: $\{\lambda < 0.05, \theta_{off}^{FE} = \theta_{off}^{RUD} \approx 10^\circ, \theta_{off}^{PS} > 0\}$ would in fact reproduce the experimental data in terms of curvature of fitted surfaces. Other combinations of these parameters would produce curvatures of the fit-

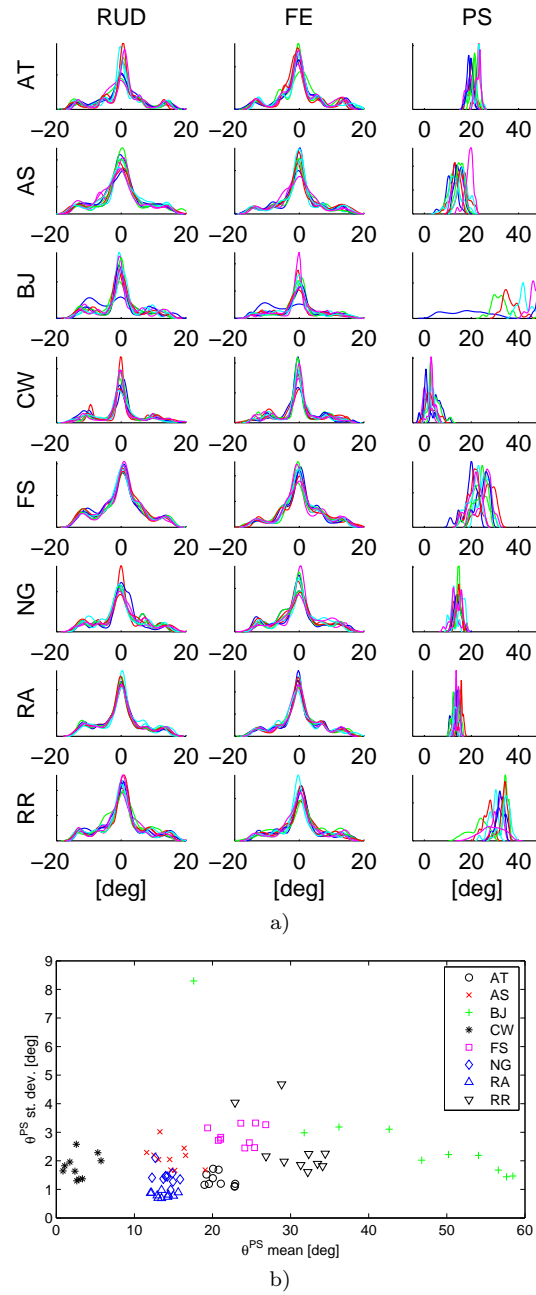


Fig. 7 Distribution of joint angles. a) presents the distribution of the three joint angles (columns) for all subjects (rows) across all trials, where each line corresponds to one trial. b) shows the distribution of the PS joint of each subject when all trials are grouped together.

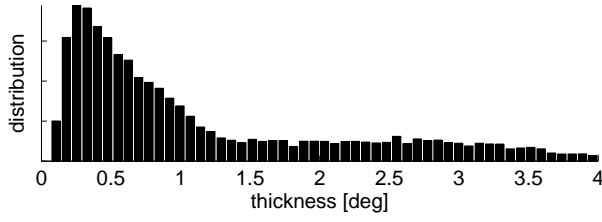


Fig. 8 Normalized distribution of the thickness values for the simulated data for systematic variations of the model parameters ($0 \leq \lambda \leq 0.2$, RUD and FE offsets within $\pm 20^\circ$, PS offset within $\pm 40^\circ$).

ting surfaces beyond the areas of the *HK* plot covered by the experimental data.

We further investigated the effect of λ on the shape of synthetic Donders' surfaces. Fig. 9 shows the shape index distribution of surfaces generated for values of λ ranging from 0 to 0.2 (distributions for higher values of λ tend to an impulse at $S = 0$), for PS offsets varying within a $\pm 40^\circ$ range in 10° steps, and RUD and FE offsets varying within a $\pm 20^\circ$ range in 2.5° steps. For $\lambda = 0$, i.e. when only the intrinsic cost is taken into account in eq. (12), the shape index is ≥ -0.5 . However, considering also the extrinsic costs (i.e. with $\lambda = 0.01$) allows extending the range to more negative values of the shape index as in the experimental data.

Also note in Fig. 9 that the positive range of PS offsets generates shape indexes mainly in the negative range (while a similar negative range of PS offsets yields a symmetric positive shape index range). This is consistent with experimental data for which the shape index is mainly distributed in the negative range (see Fig. 6b), whereas the range of estimated PS joint angles (and thus also the PS offset, see below) is strictly positive (see Fig. 7a,b).

We also analyzed how the parameter λ influences the distribution of PS joint angles predicted by our model. In particular, the RUD and FE offsets were set at 10° , a value heuristically found to reproduce physiological curvatures, and the PS offset θ_{off}^{PS} was set from 0° to 40° in five 10° steps. We then varied λ from 0 to 1, and for each simulated trial we computed mean and standard deviation (SD) of the PS joint angle (Fig. 10). For $\lambda = 0$ only the intrinsic cost is considered in eq. (12), thus the mean PS joint angle will coincide with the most comfortable position θ_{off}^{PS} . When $\lambda = 1$ only the extrinsic cost is considered in eq. (12), thus θ_{off}^{PS} has no influence. As λ increases, the mean values for the PS joint angle will therefore tend more towards 0° .

The lower plot of Fig. 10 shows that the standard deviation of the PS joint angle, i.e. the relative involvement of the PS joint in the task, is rather insensitive to the PS offset and decreases as λ increases. This is consistent with the experimental data in Fig. 7b, as the subjects' data exhibit a standard deviation of the PS joint angle around $1\text{--}3^\circ$, while the mean of the PS joint angle distribution greatly varies from subject to subject. The experimental standard deviation of the PS joint angle, i.e. the relative involvement of the

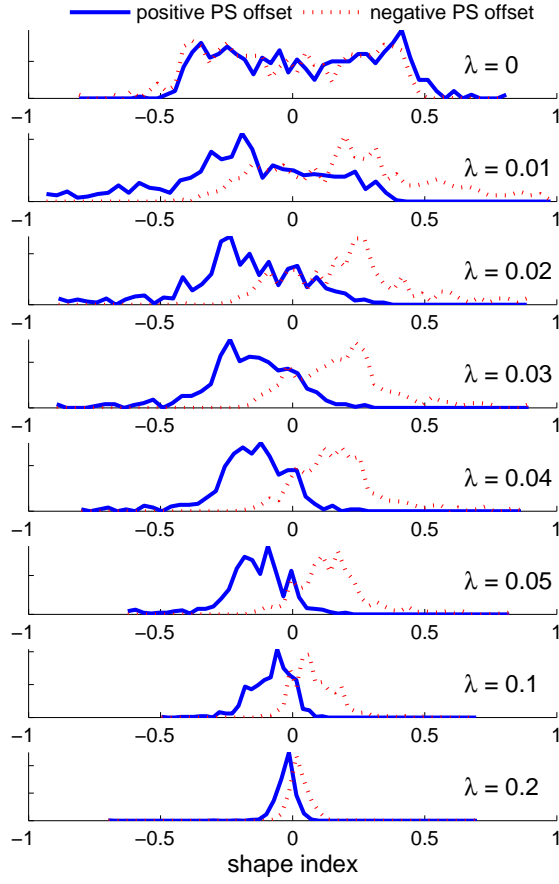


Fig. 9 Shape index distribution for $0 \leq \lambda \leq 0.2$. In each plot the offset values for FE and RUD are systematically varied within $\pm 20^\circ$ while the PS offset (θ_{off}^{PS}) is varied between 0° and $+40^\circ$ (solid lines) and between -40° and 0° (dashed lines).

PS joint in the task, is indicative of suitable values for λ in the model, i.e. the relative weight of intrinsic costs with respect to task-related costs in eq. (12). In particular, from the lower plot of Fig. 10 the standard deviation found experimentally is compatible with λ values approximately around 0.02.

5 Discussion

The main goal of this study was to propose an explanation for the geometric, subject-specific features experimentally observed in Donders' laws relative to

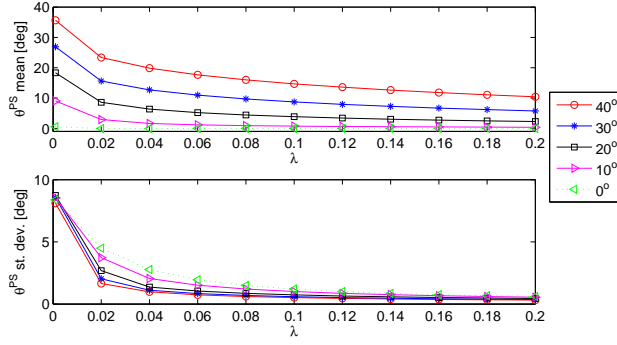


Fig. 10 Effect of λ on the mean (top) and standard deviation (bottom) of the PS joint angle (θ^{PS}) during one trial for different values of PS offset (as in legend), while $\theta_{off}^{RUD} = \theta_{off}^{FE} = 10^\circ$. As $\lambda \rightarrow 1$, both mean and standard deviation of θ^{PS} tend to zero.

pointing tasks with the human wrist, in the form of a simple computational model.

We first recorded human subjects performing wrist movements from a central position on a screen to eight peripheral targets 15° away from the central one. In line with previous work [3], the results first confirmed the existence of a reproducible relation between the forearm pronation/supination, wrist flexion/extension and wrist radial-ulnar deviation solely dependent on the pointing direction, i.e. a Donders' law. For each subject, the 3-dimensional rotation vectors describing the wrist configuration could be well fitted by a second order (Donders') surface. Furthermore, we found subject-specific features of the Donders' surface such as distinct biases in the forearm pronosupination and distinct curvatures and shapes.

Donders' law is a particular form of motor synergy that would be used by the brain to simplify problems where kinematic redundancy is involved. Listing found that, in gazing, such a synergy is characterized by a planar Donders' surface. It was also recently hypothesized that reference frames for the eye might be projected on the upper limb and used to plan arm movements as well, which would simplify visuo-motor coordination [14], [2]. In particular, the wrist has the same degrees-of-freedom (dof) as the eye, and may thus be controlled using similar neural mechanisms [15]. Therefore, we hypothesized that the coordination of the wrist dof might also consider minimal rotation strategies, possibly originating in the oculomotor domain.

However, the experimental Donders' surfaces for the wrist are curved. Through the proposed model, we investigated the possibility that this deviation from a Listing's plane results from biomechanics factors in the form of a preferred posture of the wrist joint angles. This yielded a simple optimization model with only four parameters: the comfortable position in each of the three wrist dofs (θ_{off}^{PS} , θ_{off}^{FE} , θ_{off}^{RUD}), and the weight (λ) between intrinsic and extrinsic costs. Concurrent minimization of the extrinsic rotation and

intrinsic deviation from the preferred joint angles was formulated using tools from Lie group theory, and could be computed via the one parametric torsion equation. This new solution of the redundancy problem for a wrist mechanism and the efficient minimization algorithm could be used to plan movements of redundant robots.

Comparison of the results from the simulated and real experiments yielded several observations. First, both intrinsic and task-related costs are necessary to obtain simulation results similar to those of human subjects. In fact, with reference to the total cost in eq.(12), neither $\lambda = 0$ (intrinsic costs only) nor $\lambda = 1$ (task-related costs only) would generate surfaces with extremal shape index values ± 0.7 , as was found in some subjects (Fig. 6-b).

A second observation is that the thickness of the data relative to the second order surface fit (standard deviation of the residuals from the fitting), which is generally assumed to be indicative of the goodness of fit, was similar in the simulation and in the experiment. While large thickness values (i.e. poorer fit) are typically associated with violations of Donders' law, our model presents an example of a perfect Donders' law which cannot be perfectly approximated by a second order surface. This shows that one should not over-interpret usual Donders' surfaces. This further suggests an alternative representation through the four parameters of our model, which could replace the usual Donders' surface representation.

A third observation emerging from the simulations is that the involvement of the PS joint during the task is indicative of the weight of extrinsic and task-related costs, i.e. the parameter λ in eq. (12). Different strategies could be deployed to perform a redundant task such as pointing. One extreme solution would consist of locking one joint, e.g. PS, and performing the task using the remaining joints, e.g. FE and RUD. However this would not be very comfortable for pointing at some of the targets due to the limited range of motion of the RUD joint. In contrast, involving the PS joint can reduce the motion of the RUD joint. The amount of involvement of each joint can be experimentally estimated, e.g. from Fig. 7, and quantified as standard deviation of the joint angle distribution. Our model predicts that the standard deviation of the PS joint angle is related to the parameter λ as in Fig. 10 (lower plot), and is rather independent from other parameters such as the PS offset.

Our model did not include gravity as we believe that its effect is negligible for pointing tasks with the wrist while grasping a lightweight handle. In fact, in contrast to experimental findings for head movements [4], neither our previous work on wrist movements [3] nor the experiments presented in this paper pointed to a Fick-like strategy, the signature for optimal movements in presence of gravity [4]. Our intrinsic cost is similar to the discomfort functions proposed by Cruse [6], [5] and Pennestrì et al. [21] for redundant arm posture and movements.

While simulations with a heuristically selected set of parameters ($\theta_{off}^{RUD} = \theta_{off}^{FE} = 10^\circ$, λ in the range of $0.01 - 0.02$ and θ_{off}^{PS} in the $0-40^\circ$ range) give a good prediction of the data of subjects performing movements at comfortable speed, our model based on static cost functions is probably not suitable to

predict fast movements. It may then be necessary to extend the present model by including dynamic modeling and costs such as effort and movement error [23], [10]. Results from our model could be seen as the outcome of a planning stage and used to determine the terminal constraints of a more general cost function, as proposed by Guigon [11].

6 Acknowledgement

This study was partially funded by the Academic Research Fund (AcRF) Tier1 (RG 40/09), Ministry of Education, Singapore, and by the EU FP7 VI-ACTORS project. The authors are grateful to Ms Kelly Savin for proofreading the manuscript.

A Notations for wrist orientation

A.1 Endpoint space representations

The 3D orientation of a rigid body such as the human wrist can be described by means of a 3×3 rotation matrix R (satisfying ortho-normality $R^T R = I$ and ‘right-handedness’ $\det R = +1$). A rotation is physically determined once the rotation axis \mathbf{n} ($|\mathbf{n}| = 1$) and the rotation angle θ are known, thus can be described by a rotation vector $\mathbf{r} = \theta \mathbf{n}$.

The rotation matrix R corresponding to a rotation vector \mathbf{r} can be computed via the Rodrigues’ formula [20]:

$$R = \exp(\hat{\mathbf{r}}) = I + \sin|\mathbf{r}| \frac{\hat{\mathbf{r}}}{|\mathbf{r}|} + (1 - \cos|\mathbf{r}|) \frac{\hat{\mathbf{r}}^2}{|\mathbf{r}|^2}, \quad (\text{A-1})$$

where the skew-symmetric matrix $\hat{\mathbf{r}}$ is defined through:

$$\hat{\cdot} : \mathbf{r} = \begin{bmatrix} r_x \\ r_y \\ r_z \end{bmatrix} \longrightarrow \begin{bmatrix} 0 & -r_z & r_y \\ r_z & 0 & -r_x \\ -r_y & r_x & 0 \end{bmatrix} = \hat{\mathbf{r}}.$$

Conversely, for a given rotation matrix R , the corresponding rotation vector can be computed as:

$$\mathbf{r} = \log_{\vee}(R) = \frac{\theta}{2 \sin \theta} \begin{bmatrix} R_{3,2} - R_{2,3} \\ R_{1,3} - R_{3,1} \\ R_{2,1} - R_{1,2} \end{bmatrix} \quad (\text{A-2})$$

where $\theta = \arccos((\text{trace}(R) - 1)/2)$, valid for $\theta < \pi$.

A.2 Forward kinematics

Following the axes conventions of [26], the wrist orientation R can be computed as the ordered product of three rotations:

$$R(\boldsymbol{\theta}) = \exp(-\hat{\mathbf{e}}_x \theta^{PS}) \exp(\hat{\mathbf{e}}_z \theta^{FE}) \exp(\hat{\mathbf{e}}_y \theta^{RUD}) \quad (\text{A-3})$$

and the corresponding rotation vector is:

$$FK(\boldsymbol{\theta}) := \log_{\vee}(R(\boldsymbol{\theta})). \quad (\text{A-4})$$

A.3 Inverse kinematics

If the wrist orientation is given by the rotation matrix R , the joint angles $\theta = [\theta^{RUD} \ \theta^{FE} \ \theta^{PS}]^T$ can be computed as the Euler angles [22]. Although, in general there are several solutions, the biomechanical range of motion of the wrist (see Table 1) yields a unique joint angles configuration for any reachable orientation:

$$IK(\mathbf{r}) = \theta = \begin{bmatrix} \text{atan2}(R_{1,3}, R_{1,1}) \\ \arcsin(-R_{1,2}) \\ \text{atan2}(-R_{3,2}, R_{2,2}) \end{bmatrix}. \quad (\text{A-5})$$

References

1. Andrews JG, Youm Y (1979) A biomechanical investigation of wrist kinematics. *J Biomechanics* 12:83-93
2. Blohm G, Crawford JD (2007) Computations for geometrically accurate visually guided reaching in 3-D space. *Journal of Vision* 7(5):4, 1-22
3. Campolo D, Formica D, Guglielmelli E, Keller F (2010) Kinematic analysis of the human wrist during pointing tasks. *Exp Brain Res* 201:561-573
4. Ceylan M, Henriques DYP, Tweed DB, Crawford JD (2000) Task dependent constraints in motor control: pinhole goggles make the head move like an eye. *J Neurosci* 20:2719-2730
5. Cruse H, Wischmeyer E, Bruwer M, Brockfeld P, Dress A (1990) On the Cost Functions for the Control of the Human Arm Movement. *Biol Cybernetics* 62:519-528.
6. Cruse H (1986) Constraints for Joint Angle Control of the Human Arm. *Biol Cybern* 54:125-132
7. Do Carmo MP (1976) *Differential Geometry of Curves and Surfaces*. Prentice Hall, New Jersey
8. Donders FC (1847) Beitrag zur Lehre von den Bewegungen des menschlichen Auges. *Holland Beitr Anat Physiol Wiss* 1:104-145
9. Engelbrecht SE (2001) Minimum Principles in Motor Control. *J Mathematical Psychology* 45, 497-542
10. Franklin DW, Burdet E, Tee KP, Osu R, Chew CM, Milner TE, Kawato M (2008) CNS Learns Stable, Accurate, and Efficient Movements Using a Simple Algorithm. *The Journal of Neuroscience*, 28(44):11165-11173
11. Guigon E, Baraduc P, Desmurget M (2008) Optimality, stochasticity, and variability in motor behavior. *J Comput Neurosci* 24:57-68
12. Hansard M, Horaud R (2010) Cyclorotation Models for Eyes and Cameras. *IEEE Trans Systems, Man, and Cybernetics - Part B: Cybernetics* 40:151-161
13. Hepp K (1995) Theoretical Explanations of Listing's Law and Their Implication for Binocular Vision. *Vision Res* 35:3237-3241
14. Hepp K (1990) On Listings law. *Commun Math Phys* 132:285-292
15. Hoffman DS, Strick PL (1993) Step-tracking Movements of the Wrist. III. Influence of Changes in Load on Patterns of Muscle Activity. *J Neuroscience* 13(12):5212-5227
16. Hore J, Watts S, Vilis T (1992) Constraints on arm position when pointing in three dimensions: Donders law and the Fick-gimbal strategy. *J Neurophysiol*, 68:374-383
17. Koenderink JJ, van Dron AJ (1992) Surface shape and curvature scales. *Image and Vision Computing* 10:557-564
18. Leonard L, Sirkett D, Mullineux G, Giddins GEB, Miles AW (2005) Development of an in-vivo method of wrist joint motion analysis, *Clinical Biomechanics* 20:166-171
19. Montgomery R (2002) *A Tour of Subriemannian Geometries, Their Geodesics and Applications*. Mathematical Surveys and Monographs, 91. American Mathematical Society, Providence, RI. USA
20. Murray RM, Li Z, Sastry SS (1994) *A Mathematical introduction to robotic manipulation*. CRC Press, Boca Raton
21. Pennestrì E, Stefanelli R, Valentini PP, Vita L (2007) Virtual musculo-skeletal model for the biomechanical analysis of the upper limb. *J Biomechanics* 40:1350-1361

-
22. Shoemake K (1985) Animating rotation with quaternion curves. In Proc. of the 12th annual conference on Computer graphics and interactive techniques (SIGGRAPH), 16(3):245-254, San Francisco, CA, USA, Jul 22-26.
 23. Todorov E (2004) Optimality Principles in Sensorimotor Control. *Nature Neurosc* 7:907-915
 24. Tweed D, Vilis T (1990) Geometric Relations of Eye Position and Velocity Vectors during Saccades. *Vision Res* 30:111-127
 25. Wong AMF (2004) Listing's law: Clinical significance and implications for neural control, *Surv Ophthalmol* 49:563-575
 26. Wu G et al. (2005) ISB recommendation on definitions of joint coordinate systems of various joints for the reporting of human joint motion - Part II: shoulder, elbow, wrist and hand. *J Biomech* 38:981-992, 2005.